Petroleum Science 20 (2023) 2075–2091

Contents lists available at ScienceDirect

Petroleum Science

journal homepage: www.keaipublishing.com/en/journals/petroleum-science

Original Paper

The applicability and underlying factors of frequency-dependent amplitude-versus-offset (AVO) inversion

Fang Ouyang [a, b], Xin-Ze Liu [c], Bin Wang [a], Zi-Duo Hu [d], Jian-Guo Zhao [a, e, *], Xiu-Yi Yan [f, **], Yu Zhang [a], Yi-He Qing [a]

[a] State Key Laboratory of Petroleum Resource and Prospecting, China University of Petroleum (Beijing), Beijing, 102249, China
[b] Institute of Earthquake Forecasting, China Earthquake Administration, Beijing, 100036, China
[c] Yumen Oil Field Branch of CNPC Exploration and Development Research Institute, Jiuquan, Gansu, 735000, China
[d] Northwest Branch of PetroChina Research Institute of Petroleum Exploration and Development, Lanzhou, Gansu, 730020, China
[e] Unconventional Petroleum Research Institute, China University of Petroleum (Beijing), Beijing, 102249, China
[f] College of Chemical Engineering and Environment, China University of Petroleum (Beijing), Beijing, 102249, China

ARTICLE INFO

Article history:
Received 28 May 2022
Received in revised form
1 November 2022
Accepted 14 February 2023
Available online 16 February 2023

Edited by Jie Hao

Keywords:
Zoeppritz approximation
Dispersion gradient
Frequency-dependent AVO inversion
Reservoir prediction
Fluid identification

ABSTRACT

Recently, the great potential of seismic dispersion attributes in oil and gas exploration has attracted extensive attention. The frequency-dependent amplitude versus offset (FAVO) technology, with dispersion gradient as a hydrocarbon indicator, has developed rapidly. Based on the classical AVO theory, the technology works on the assumption that elastic parameters are frequency-dependent, and implements FAVO inversion using spectral decomposition methods, so that it can take dispersive effects into account and effectively overcome the limitations of the classical AVO. However, the factors that affect FAVO are complicated. To this end, we construct a unified equation for FAVO inversion by combining several Zoeppritz approximations. We study and compare two strategies respectively with (strategy 1) and without (strategy 2) velocity as inversion input data. Using theoretical models, we investigate the influence of various factors, such as the Zoeppritz approximation used, P- and S-wave velocity dispersion, inversion input data, the strong reflection caused by non-reservoir interfaces, and the noise level of the seismic data. Our results show that FAVO inversion based on different Zoeppritz approximations gives similar results. In addition, the inversion results of strategy 2 are generally equivalent to that of strategy 1, which means that strategy 2 can be used to obtain dispersion attributes even if the velocity is not available. We also found that the existence of non-reservoir strong reflection interface may cause significant false dispersion. Therefore, logging, geological, and other relevant data should be fully used to prevent this undesirable consequence. Both the P- and S-wave related dispersion obtained from FAVO can be used as good indicators of a hydrocarbon reservoir, but the P-wave dispersion is more reliable. In fact, due to the mutual coupling of P- and S-wave dispersion terms, the P-wave dispersion gradient inverted from PP reflection seismic data has a stronger hydrocarbon detection ability than the S-wave dispersion gradient. Moreover, there is little difference in using post-stack data or pre-stack angle gathers as inversion input when only the P-wave dispersion is desired. The real application examples further demonstrate that dispersion attributes can not only indicate the location of a hydrocarbon reservoir, but also, to a certain extent, reveal the physical properties of reservoirs.

1. Introduction

The amplitude-versus-offset (AVO) analysis technology is one of the most widely used techniques in oil exploration and production (Ostrander, 1984; Smith and Gidlow, 1987; Russell et al., 2003). For such amplitude-dependent techniques, parameters such as the AVO type, intercept, and gradient are determined by analyzing

* Corresponding author. State Key Laboratory of Petroleum Resource and Prospecting, China University of Petroleum (Beijing), Beijing, 102249, China.
** Corresponding author.
E-mail addresses: zhaojg@cup.edu.cn (J.-G. Zhao), yanxiuyi@cup.edu.cn (X.-Y. Yan).

https://doi.org/10.1016/j.petsci.2023.02.011

amplitude variations in the reflection coefficient against the offset/incident angle, and these parameters are then used to identify the "bright spots" of hydrocarbon reservoirs (Castagna et al., 1998; Avseth et al., 2001; Wei et al., 2008; Pan et al., 2016). During the past years, the AVO technique has long been the most convincing tool for predicting lithology and fluid attributes. However, this classical technique does not account for dispersive effects, thus exhibiting limitations in the accurate prediction of fluid distributions for lithologic and deep-water reservoirs. In fact, a large number of studies have illustrated that the amplitude of a seismic wave reflection is not only related to its incident angle, but also its frequency (Chapman et al., 2006; Guo et al., 2015, 2016). For hydrocarbon-bearing reservoir rocks in particular, the existence of pore fluids will lead to different degrees of seismic wave dispersion and attenuation (Batzle et al., 2006; Ludmila and Batzle, 2008; Chen et al., 2016a, 2016b). This variability is important, as it forms the basis for using seismic dispersion and attenuation attributes to predict reservoirs and identify fluids (Castagna et al., 2003; Ebrom, 2004; Rapoport et al., 2004; Odebeatu et al., 2006; Zong et al., 2015; Chen, 2020; Chen et al., 2021). Recently, with the development of petrophysics and high-precision spectral decomposition technologies, using seismic dispersion as a fluid indicator in hydrocarbon detection has garnered a substantial amount of research interest (Partyka, 1999; Castagna et al., 2003; Korneev et al., 2004; Sinha et al., 2009). The corresponding frequency-dependent AVO (FAVO) technology has also developed rapidly (Wilson et al., 2009; Zhang et al., 2011; Chen et al., 2015; Zong et al., 2016; Liu et al., 2019).

FAVO predicts fluid properties and distributions by taking the dispersion gradient as a hydrocarbon indicator. The technology works on the assumption that model parameters are frequency dependent, and implements the AVO inversion based on Zoeppritz approximate equations and time-frequency analysis techniques. FAVO has recently gone through three stages of development, namely, frequency division recognition, frequency division AVO analysis, and frequency-dependent AVO inversion. The frequency division recognition stage is mainly characterized by the discovery of "low frequency shadow" (Castagna et al., 2003; Chen et al., 2009). Castagna et al. (2003) found that the energy mass below a gas-bearing reservoir gradually decreases and then disappears with increasing frequency, and this is known as the "low frequency shadow" phenomenon. Ren et al. (2007, 2009) then showed that changes in a formation's lithology and fluid properties represent important influences on the distribution of seismic energy in the frequency domain. Following these discoveries, a spectra cross-plot technique was developed for frequency division AVO analysis. This technique utilizes spectral decomposition at different incident angles and discriminates gas from wet reservoirs by integrating AVO and frequency-dependent analysis (Ren et al., 2007). However, the spectra cross-plot method used in frequency division AVO is qualitative. The physical mechanisms of the seismic dispersion generated by hydrocarbon reservoirs are still not fully understood. To further investigate the AVO response of hydrocarbon deposits, Chapman et al. (2006) combined the AVO theory with rock physics based on a squirt model, and studied reflections from the interface between an elastic overburden and a dispersive equivalent medium with frequency-dependent velocity and attenuation. They found that the reflection coefficient at the interface exhibits apparent frequency dependency; and that this frequency response is coupled to AVO behavior. Using field examples, Goloshubin et al. (2006) also discovered that oil-rich reservoirs can enhance reflection energy at the low frequencies. Meanwhile, Batzle et al. (2006) identified significant differences in the dispersion behavior of rocks saturated with different fluids based on rock physics experiments.

In light of this, Wilson et al. (2009) modified the Zoeppritz approximate expression proposed by Smith and Gidlow (1987), and added the influence of velocity dispersion to the classical AVO theory. They assumed that the impedance contrast is frequency-related, and developed the first spectral-decomposition-based inversion algorithm to extract dispersion attributes. Wilson et al. (2009)'s work lays an important theoretical foundation for the FAVO inversion. Wu et al. (2010) then combined the Wigner-Ville distribution spectral decomposition with the FAVO technique (Wilson et al., 2009), and applied the method to real seismic field data. Based on the Bayesian method, Wu et al. (2015) further applied the FAVO technique in the quantitative prediction of gas saturation and reservoir porosity. Zhang et al. (2011) then re-deduced the FAVO equation following the Shuey approximation (Shuey, 1985), and classified the velocity term into the dispersion gradient as a parameter to be inverted. Compared with the method proposed by Wilson et al. (2009), this approach can obtain the seismic dispersion even if the velocity is not available, making it very convenient for practical applications. To extract high-resolution time–frequency depiction, Huang et al. (2017) and Liu et al. (2018) respectively combined the FAVO inversion with sparse constrained inversion spectral decomposition and variational model decomposition. Many other studies have also proven that FAVO is both effective and practical, and performs well in the detection of subtle reservoir and fluid properties (Cheng et al., 2012; Zhang et al., 2014; Pang et al., 2018; Liu et al., 2019; Kumar et al., 2019; Ajaz et al., 2021; Qin et al., 2021). However, factors that affect the effectiveness of FAVO inversion are complex, such as the selection of Zoeppritz approximation equations, the influence of dispersive P- and S-wave velocities, the calculation of the spectrum balance coefficient, the side effects of strong reflection from non-reservoir interfaces, and the noise level of the seismic data. Few studies have investigated how and to what degree these factors affect FAVO inversion.

To address the abovementioned issues, here a unified equation for FAVO inversion is presented with reference to several classical Zoeppritz approximate equations. Two inversion strategies, whose input either did (strategy 1) or did not (strategy 2) involve velocity, are reviewed and compared. On this basis, the influence of the factors mentioned above on the results of FAVO inversion are then investigated using a theoretical model. By applying the FAVO inversion to real seismic field data, we further verify the reliability and practicability of the technique.

2. Methods

2.1. Classical zoeppritz approximations

The Zoeppritz approximation equation forms the mathematical foundation of FAVO inversion. At present, commonly used Zoeppritz approximations include the Aki-Richard, Smith-Gidlow, Rüger, Gary, and Goodway approximations. The expressions of these approximations are as follows.

According to Aki and Richards (2009), the PP reflection coefficient can be approximately expressed as:

$$R(\theta) \approx \frac{1}{2\cos^2\theta}\frac{\Delta V_P}{\overline{V}_P} - 4\frac{\overline{V}_S^2}{\overline{V}_P^2}\sin^2\theta\frac{\Delta V_S}{\overline{V}_S} + \left(\frac{1}{2} - 2\frac{\overline{V}_S^2}{\overline{V}_P^2}\sin^2\theta\right)\frac{\Delta\rho}{\overline{\rho}} \tag{1}$$

According to Smith and Gidlow (1987), the PP reflection coefficient is given by:

$$R(\theta) \approx \left(\frac{5}{8} - \frac{1}{2}\frac{\overline{V}_S^2}{\overline{V}_P^2}\sin^2\theta + \frac{1}{2}\tan^2\theta\right)\frac{\Delta V_P}{\overline{V}_P} - 4\frac{\overline{V}_S^2}{\overline{V}_P^2}\sin^2\theta\frac{\Delta V_S}{\overline{V}_S} \quad (2)$$

According to Rüger (2002), the expression for isotropic media is as follows:

$$R(\theta) \approx \frac{1}{2}\frac{\Delta I_P}{\overline{I}_P} + \frac{1}{2}\left[\frac{\Delta V_P}{\overline{V}_P} - 4\left(\frac{\overline{V}_S}{\overline{V}_P}\right)^2\frac{\Delta\mu}{\overline{\mu}}\right]\sin^2\theta \quad (3)$$

According to Gray et al. (1999), the expression is:

$$R(\theta) \approx \frac{1}{2}\left(\frac{1}{2} - \frac{\overline{V}_S^2}{\overline{V}_P^2}\right)\frac{1}{\cos^2\theta}\frac{\Delta\lambda}{\overline{\lambda}} + \frac{\overline{V}_S^2}{\overline{V}_P^2}\left(\frac{1}{2\cos^2\theta} - 2\sin^2\overline{\theta}\right)\frac{\Delta\mu}{\overline{\mu}} + \frac{1}{2}\left(1 - \frac{1}{2\cos^2\theta}\right)\frac{\Delta\rho}{\overline{\rho}} \quad (4)$$

According to Goodway (1997), the PP reflection coefficient has the following form:

$$R(\theta) \approx \frac{1}{2}\left(1 + \tan^2\theta\right)\frac{\Delta I_P}{\overline{I}_P} - 4\frac{\overline{V}_S^2}{\overline{V}_P^2}\sin^2\theta\frac{\Delta I_S}{\overline{I}_S} - \left(\frac{1}{2}\tan^2\theta - 2\frac{\overline{V}_S^2}{\overline{V}_P^2}\sin^2\theta\right)\frac{\Delta\rho}{\overline{\rho}} \quad (5)$$

where R is the PP reflection coefficient, θ is the incident angle, $\Delta V = V_2 - V_1$ and $\Delta\rho = \rho_2 - \rho_1$ are the velocity and density differences between the upper and lower layers respectively (as shown in Fig. 1), the subscripts "S" and "P" denote shear and compressional waves respectively, $\overline{V} = (V_2 + V_1)/2$ and $\overline{\rho} = (\rho_2 + \rho_1)/2$ are the average velocity and density between the upper and lower layers respectively, $I_P = \rho V_P$ and $I_S = \rho V_S$ are the P-wave and S-wave impedances respectively, μ is the shear modulus, and λ is the Lamé constant.

2.2. FAVO inversion equation

Based on the classical Zoeppritz approximations above, a unified form of the FAVO inversion equation is established for each of two strategies: strategy 1, in which the velocity is considered as a known parameter (e.g., Wilson et al., 2009), and strategy 2, in which the velocity is regarded as an unknown parameter (e.g., Zhang et al., 2011). Taking the Aki-Richard approximation as an example, the specific implementation of the two strategies is introduced in this section. The other approximations can then be obtained in a similar way.

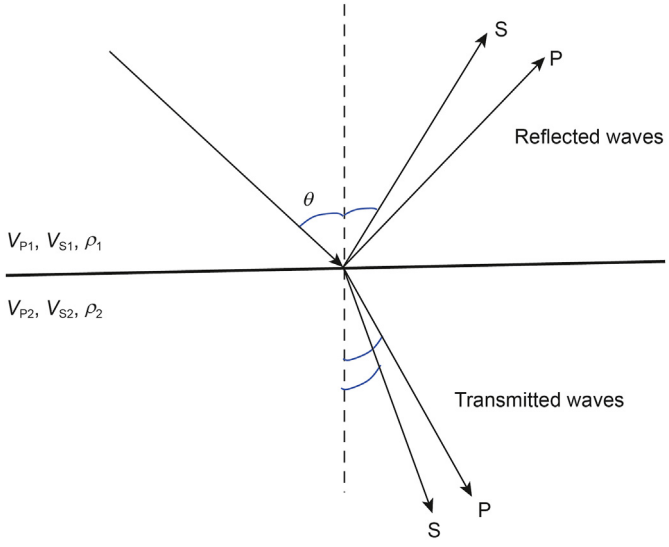

Fig. 1. Reflection and transmission at a single interface.

(1) Inversion Strategy 1

Assuming that the velocity is known, the Aki-Richard approximate Eq. (1) can be transformed as follows:

$$R(\theta) \approx A(\theta)X + B(\theta)Y + C(\theta)P \quad (6)$$

where $C(\theta) = 0.5 - 2\sin^2\theta\overline{V}_S^2\overline{V}_P^{-2}$, $P = \Delta\rho/\overline{\rho}$ and A, B are given by Table 1. $X = \Delta V_P/\overline{V}_P$ and $Y = \Delta V_S/\overline{V}_S$ are the P- and S-wave velocity contrast, respectively. For other Zoeppritz approximation equations, the parameters A, B, X, Y can also be found in Table 1. Note that in strategy 1, the P- and S-wave velocities are known.

As the velocity varies with frequency f, X and Y can then be expressed as functions of frequency as follows:

$$R(\theta, f) \approx A(\theta)X(f) + B(\theta)Y(f) + C(\theta)P \quad (7)$$

At the reference frequency $f = f_0$, applying Taylor expansion to the above equation delivers the following result:

$$\Delta R(\theta, f) = (f - f_0)[A(\theta)\mathrm{d}X(f_0) + B(\theta)\mathrm{d}Y(f_0)] \quad (8)$$

where $\Delta R(\theta, f) = R(\theta, f) - R(\theta, f_0)$, with $R(\theta, f_0) = A(\theta)X(f_0) + B(\theta)Y(f_0) + C(\theta)P$; $\mathrm{d}X = \partial X/\partial f$ and $\mathrm{d}Y = \partial Y/\partial f$ represent the dispersion terms. The P- and S-wave related dispersion gradients D_P and D_S can then be obtained from $\mathrm{d}X$ and $\mathrm{d}Y$ using the relationships shown in Table 1.

(2) Inversion Strategy 2

For actual seismic data, the velocity is usually unknown. In such cases, the dispersion gradient attributes can be inverted by replacing the parameter $Y = \Delta V_S/\overline{V}_S$ in Eq. (7) with $Y = \overline{V}_S^2\overline{V}_P^{-2}\cdot\Delta V_S/\overline{V}_S$ (also see the parameters for strategy 2 in Table 1). Consequently, the coefficients A and B for strategy 2 become:

$$A(\theta) = 0.5\cos^{-2}\theta, B(\theta) = -4\sin^2\theta \quad (9)$$

As can be seen, the inversion equations of strategies 1 and 2 are completely consistent, just as shown in Eq. (8). The only difference lies in the specific form and significance of parameters A, B, X, and Y.

Considering M depth (or time) sampling points, N angles, and L frequency sampling points, Eq. (8) can be further formatted into matrices:

Table 1
Coefficients A and B and inversion parameters X and Y for different Zoeppritz approximations.

Approximation	Strategy 1	Strategy 2
Aki-Richard	$X = D_P = \Delta V_P/\overline{V}_P$ $Y = D_S = \Delta V_S/\overline{V}_S$ $A(\theta) = 0.5\cos^{-2}\theta$ $B(\theta) = -4\sin^2\theta\overline{V}_S^2\overline{V}_P^{-2}$	$X = D_P = \Delta V_P/\overline{V}_P$ $Y = D_S = \overline{V}_S^2\overline{V}_P^{-2}\cdot\Delta V_S/\overline{V}_S$ $A(\theta) = 0.5\cos^{-2}\theta$ $B(\theta) = -4\sin^2\theta$
Smith-Gidlow	$X = D_P = \Delta V_P/\overline{V}_P$ $Y = D_S = \Delta V_S/\overline{V}_S$ $A(\theta) = 5/8 + 0.5\tan^2\theta - 0.5\overline{V}_S^2\overline{V}_P^{-2}\sin^2\theta$ $B(\theta) = -4\overline{V}_S^2\overline{V}_P^{-2}\sin^2\theta$	$X = D_P = \Delta V_P/\overline{V}_P$ $Y = (X/8 + \Delta V_S/\overline{V}_S)\overline{V}_S^2\overline{V}_P^{-2}$ $D_S = Y - X/32$ $A(\theta) = 5/8 + 0.5\tan^2\theta$ $B(\theta) = -4\sin^2\theta$
Rüger	$X = D_P = \Delta I_P/\overline{I}_P$ $Y = \Delta V_P/\overline{V}_P, Z = D_S = \Delta\mu/\overline{\mu}$ $A(\theta) = 0.5, B(\theta) = 0.5\sin^2\theta$ $C(\theta) = -2\overline{V}_S^2\overline{V}_P^{-2}\sin^2\theta$	$X = D_P = \Delta I_P/\overline{I}_P$ $Y = 4\overline{V}_S^2\overline{V}_P^{-2}\Delta\mu/\overline{\mu} - \Delta V_P/\overline{V}_P$ $D_S = Y/4$ $A(\theta) = 0.5$ $B(\theta) = -0.5\sin^2\theta$
Gary	$X = \Delta\lambda/\overline{\lambda}$ $Y = D_S = \Delta\mu/\overline{\mu}$ $D_P = (Y + X)/4$ $A(\theta) = 0.5(0.5 - \overline{V}_S^2\overline{V}_P^{-2})\cos^{-2}\theta$ $B(\theta) = (0.5\cos^{-2}\theta - 2\sin^2\theta)\overline{V}_S^2\overline{V}_P^{-2}$	$X = D_P = 0.5\Delta\lambda/\overline{\lambda} + \overline{V}_S^2\overline{V}_P^{-2}(\Delta\mu/\overline{\mu} - \Delta\lambda/\overline{\lambda})$ $Y = D_S = \Delta\mu/\overline{\mu}$ $A(\theta) = 0.5\cos^{-2}\theta$ $B(\theta) = -2\sin^2\theta$
Goodway	$X = D_P = \Delta I_P/\overline{I}_P$ $Y = D_S = \Delta I_S/\overline{I}_S$ $A(\theta) = 0.5\cos^{-2}\theta$ $B(\theta) = -4\sin^2\theta\overline{V}_S^2\overline{V}_P^{-2}$	$X = D_P = \Delta I_P/\overline{I}_P$ $Y = D_S = \Delta I_S/\overline{I}_S\cdot\overline{V}_S^2\overline{V}_P^{-2}$ $A(\theta) = 0.5\cos^{-2}\theta$ $B(\theta) = -4\sin^2\theta$

$$\begin{pmatrix} \Delta\mathbf{R}(\theta_1,f_1) \\ \Delta\mathbf{R}(\theta_2,f_1) \\ \vdots \\ \Delta\mathbf{R}(\theta_N,f_1) \\ \Delta\mathbf{R}(\theta_1,f_2) \\ \vdots \\ \Delta\mathbf{R}(\theta_N,f_2) \\ \vdots \\ \Delta\mathbf{R}(\theta_1,f_L) \\ \vdots \\ \Delta\mathbf{R}(\theta_N,f_L) \end{pmatrix} = \begin{pmatrix} \tilde{\mathbf{A}}(\theta_1,f_1) & \tilde{\mathbf{B}}(\theta_1,f_1) \\ \tilde{\mathbf{A}}(\theta_2,f_1) & \tilde{\mathbf{B}}(\theta_2,f_1) \\ \vdots & \vdots \\ \tilde{\mathbf{A}}(\theta_N,f_1) & \tilde{\mathbf{B}}(\theta_N,f_1) \\ \tilde{\mathbf{A}}(\theta_1,f_2) & \tilde{\mathbf{B}}(\theta_1,f_2) \\ \vdots & \vdots \\ \tilde{\mathbf{A}}(\theta_N,f_2) & \tilde{\mathbf{B}}(\theta_N,f_2) \\ \vdots & \vdots \\ \tilde{\mathbf{A}}(\theta_1,f_L) & \tilde{\mathbf{B}}(\theta_1,f_L) \\ \vdots & \vdots \\ \tilde{\mathbf{A}}(\theta_N,f_L) & \tilde{\mathbf{B}}(\theta_N,f_L) \end{pmatrix} \begin{pmatrix} \mathrm{d}\mathbf{X} \\ \mathrm{d}\mathbf{Y} \end{pmatrix} \tag{10}$$

where $\Delta\mathbf{R}$, $\mathrm{d}\mathbf{X}$, and $\mathrm{d}\mathbf{Y}$ are column vectors of $M\times 1$. $\tilde{\mathbf{A}}$ and $\tilde{\mathbf{B}}$ are matrices of $M\times M$ with $\tilde{\mathbf{A}} = (f - f_0)A(\theta)\mathbf{I}$ and $\tilde{\mathbf{B}} = (f - f_0)B(\theta)\mathbf{I}$, where $\mathbf{I}$ is the unit matrix of $M\times M$. We obtain the dispersion gradients $\mathrm{d}\mathbf{X}$ and $\mathrm{d}\mathbf{Y}$ using the above inversion equations by the singular value decomposition method. Then, the P- and S-wave related dispersion gradients are obtained from $\mathrm{d}\mathbf{X}$ and $\mathrm{d}\mathbf{Y}$. The inversion equations for the other Zoeppritz approximations have forms that are consistent with that of Eq. (10). It is only necessary to change the parameters of each equation (such as A, B, X, and Y) according to Table 1.

2.3. Procedure for FAVO inversion

The main steps of frequency-dependent AVO inversion include spectral decomposition, spectrum balance, and dispersion gradient inversion. These steps can be explained as follows.

(1) Spectral decomposition is performing a time-frequency decomposition of amplitude-preserving seismic records using time-frequency analysis methods. Time-frequency analysis is a significant technique for extracting dispersion attributes from seismic data. Moreover, selecting an appropriate time-frequency analysis method is very important for frequency-dependent AVO inversion. Currently, spectral decomposition technologies are relatively mature and have been widely applied. These technologies include short-time Fourier transform, wavelet transform, S transform, Gabor transform, and the smooth pseudo-Wigner-Ville distribution (SPWVD) method. In this study, the SPWVD method is used for spectral decomposition due to its good performance in balancing time resolution and frequency resolution. Hence, we have

$$\mathbf{u}(\theta_n) \overset{\text{SPWVD}}{\rightarrow} \mathbf{U}(\theta_n, f_l) \tag{11}$$

where $\mathbf{u}(\theta_n)$ is the angle gather corresponding to θ_n, with $\mathbf{u} = [u(t_1), u(t_2), \cdots, u(t_M)]^{\mathrm{T}}$ and $n = 1, 2, \cdots, N$. $\mathbf{U}$ is the time-frequency spectrum of $\mathbf{u}$, and f_l represents the sampling frequencies with $l = 1, 2, \cdots, L$. In addition to angle gathers, post-stack seismic data can also be used for FAVO inversion. However, the post-stack data does not take angular influences into consideration, and thus in this case only the P-wave dispersion attributes can be obtained.

(2) Spectrum balance is applied to eliminate the influence of seismic wavelet on the time-frequency spectrum. It ensures that the inversion results only reflect the dispersion characteristics of the real medium. Generally, actual seismic records are often approximated as the convolution of the seismic wavelet and the reflection coefficients. Therefore, they contain not only the reflection information, but also the influence of the seismic wavelet. The spectrum of the seismic wavelet changes with frequency and exhibits characteristics tied to dispersion, thus resulting in an overprinting effect on the seismic records. If this effect is not eliminated, the influence of the wavelet and the seismic dispersion will be mixed, making them difficult to distinguish. In addition, the inversion Eq. (10) also indicates that only the reflection coefficient is required for the FAVO inversion. Therefore, it is

necessary to eliminate the effects of the wavelet from the seismic signal, while retaining only the stratigraphic reflection information.

For this reason, the time-frequency spectrum **U** at each frequency needs to be balanced using the maximum amplitude around the elastic interface at the reference frequency f_0, that is,

$$\overline{\mathbf{U}}(\theta_n, f_l) = \mathbf{U}(\theta_n, f_l) w(f_l) \tag{12}$$

where w is the spectrum balance coefficient, which is given by

$$w(f_l) = \frac{\max\limits_{Te}[\mathbf{U}(\theta_n, f_0)]}{\max\limits_{Te}[\mathbf{U}(\theta_n, f_l)]} \tag{13}$$

where Te represents the time interval corresponding to an elastic or non-reservoir interface. It is worth noting that in order to completely eliminate the overprinting effect of the seismic wavelet, the spectrum balance coefficient must be calculated using the amplitude at the elastic or non-reservoir interface. This is because only in the case of an elastic interface, the amplitude difference of the time-frequency spectrum at different frequencies is completely caused by the seismic wavelet. Therefore, selecting an appropriate elastic interface is crucial for the spectrum balance and for the effectiveness of FAVO inversion. In particular for actual seismic data, a suitable non-reservoir interface must be selected as the elastic interface with the help of logging and geological data. Otherwise, inaccurate inversion results may be obtained.

(3) Dispersion gradient inversion is realized by solving Eq. (10). We first calculate the difference between the amplitude at each frequency and that at the reference frequency using the balanced time-frequency spectrum, as follows:

$$\Delta\mathbf{R}(\theta_n, f_l) = \overline{\mathbf{U}}(\theta_n, f_l) - \overline{\mathbf{U}}(\theta_n, f_0) \tag{15}$$

Then, the singular value decomposition method is utilized to obtain the dispersion gradients.

3. Analyses based on theoretical models

In this section, we investigate the factors that affect the accuracy of FAVO inversion using a wedge-layered model illustrated in Fig. 2. In the model, the first and second layers are elastic media, while the wedge-shaped regions of the upper and lower halves of the last layer are dispersive and elastic media, respectively. The density of the dispersive medium is 2.6 g cm^{-3}, and the velocity dispersion curves of the P- and S-waves are shown on the right-hand side of Fig. 2. The Ricker wavelet with a dominant frequency of 30 Hz is used in the test, and the synthetic seismograms of the wedge-layered model are simulated by the frequency-domain reflectivity method proposed by Liu et al. (2016). The results are shown in Fig. 3, in which Fig. 3a is the zero-offset (vertical incidence) seismic section, and Fig. 3b shows the angle gathers at Trace 300.

3.1. Zoeppritz approximations

We first investigate the influence of the Zoeppritz approximations on FAVO inversion. Strategies 1 and 2 are respectively used to invert the dispersion gradients based on the five classical Zoeppritz approximations listed in Table 1. The time-frequency spectra of the angle gathers are obtained using the SPWVD spectral decomposition technique with a time window of 0.044 s. Then, we balance the time-frequency spectra at each frequency using the maximum amplitude around the elastic interface (the corresponding time interval is 0.02–0.10 s) at the dominant frequency 30 Hz. Figs. 4 and 5 compare the time-frequency spectra of the seismic records before and after the spectrum balance. As can be seen, the amplitude at each frequency is normalized to the same level at the elastic interface after the spectrum balance, while at the dispersive interface it remains different. This is because the spectrum difference at the elastic interface is caused only by the wavelet, while that at the dispersive interface is affected by the dispersion effects of both the wavelet and the medium. The spectrum balance eliminates the effects of the seismic wavelet and maintains the dispersion attributes of the medium. Therefore, this process largely determines the reliability of the inversion results.

Using the angle gathers at Trace 300 (as shown in Fig. 3b) as the input data, we perform FAVO inversion with strategies 1 and 2, respectively. The obtained dispersion gradients are shown in Figs. 6 and 7. The dispersion gradients of P- and S-waves obtained by different Zoeppritz approximations are compared in these figures, including the Aki-Richard, Smith-Gidlow, Rüger, Gary, and Goodway approximation equations. We also introduce a factor (ζ) to quantitatively evaluate the indicating ability of the dispersion gradients obtained in different cases. For the FAVO inversion, a high dispersion gradient indicates a greater possibility of hydrocarbon. Therefore, the fluid indicating ability depends on the amplitude of the dispersion gradient, that is, the larger the dispersion gradient the better the indication ability. However, elastic layers can also cause dispersions, but only dispersion from the dispersive layer is considered "true" dispersion. Those results from the elastic layers are considered "false" dispersions due to the use of spectrum decomposition (e.g. the small dispersions around the elastic interface in Figs. 6 and 7). Therefore, to better evaluate the fluid indicating ability, we define the factor (ζ) as the ratio of the minimum peak value of the dispersion gradient in the dispersive interval to the maximum peak amplitude in the elastic interval. The maximum peak value of the dispersion gradient in the dispersive interval can also be used, but we believe it is more objective and

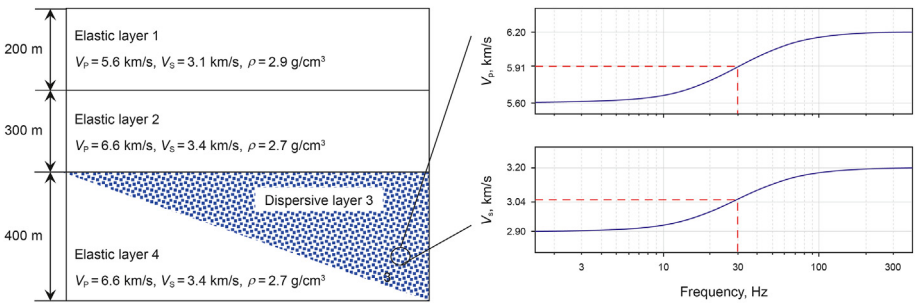

Fig. 2. Wedge-layered model.

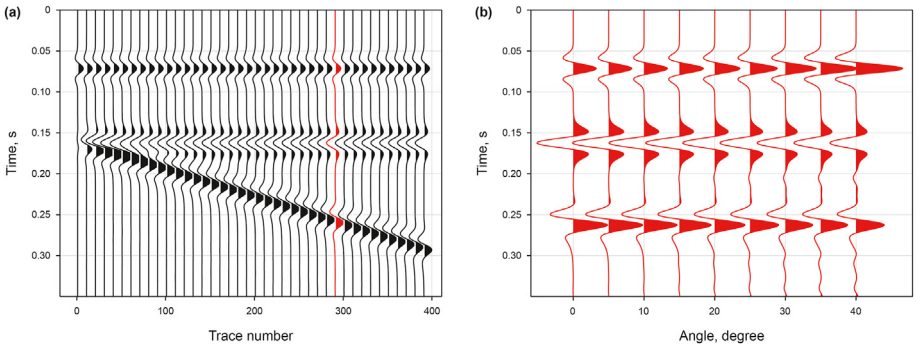

Fig. 3. Synthetic seismogram of the wedge-layered model: (a) zero-offset (vertical incidence) seismic section and (b) angle gathers at Trace 300.

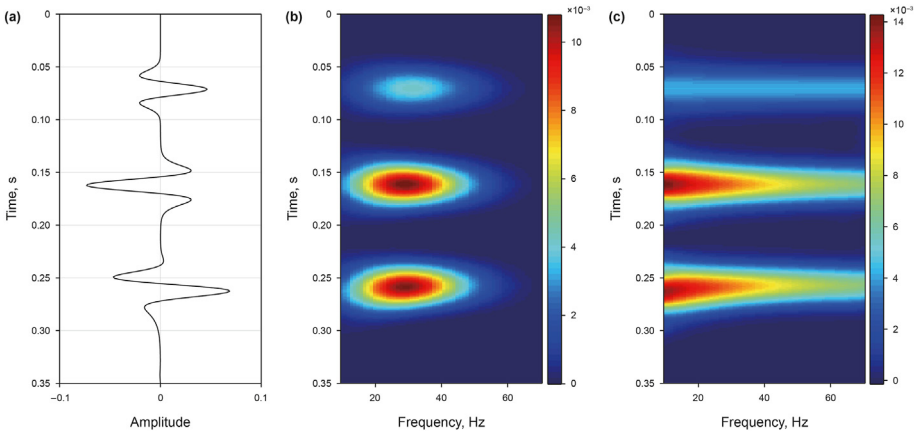

Fig. 4. The results of spectral decomposition: (a) the original seismogram, and the time-frequency spectra of the seismogram (b) before and (c) after spectrum balance.

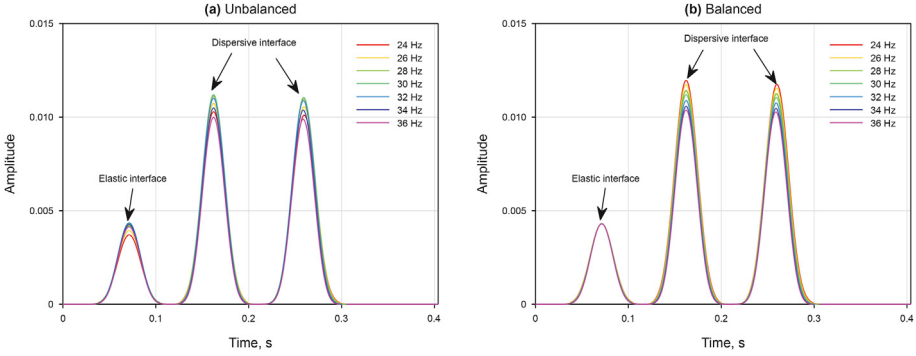

Fig. 5. Comparison of the time-frequency spectra of the seismic records at different frequencies (a) before and (b) after the spectrum balance.

reasonable to adopt the minimum one. By doing so, the magnitude of the factor (ζ) can effectively reflect the fluid indicating ability. The larger the value of ζ, the better the indicating ability. Table 2 lists the corresponding ζ values for strategies 1 and 2 based on different Zoeppritz approximations, where ζ_P and ζ_S denote the indicating ability factors for P- and S-wave dispersion gradients, respectively.

In Figs. 6 and 7, the larger dispersion gradients indicate more effective reservoir indicators. They show that the dispersion gradients obtained from the five Zoeppritz approximations exhibit apparent anomalies at the top and bottom of the dispersive layer, indicating that dispersion attributes can effectively locate reservoirs. In addition, the inversion results of the Aki-Richard and Goodway approximations agree completely and their indicating ability factors are also exactly congruent (see Table 2). This arises because the inversion equations (or parameters $A(\theta)$ and $B(\theta)$) for the two methods are essentially the same (as shown in Table 1), that is, both their velocity dispersion and wave impedance dispersion gradients are equivalent. For the sake of convenience during comparison, we normalize the inversion results using their maximum values. The normalized P-wave dispersion gradients based on different Zoeppritz approximations are almost congruent, regardless of the strategy used. However, the S-wave dispersion gradient of the Rüger equation shows an apparent inconsistency with the results from the other equations, with obvious dispersion anomalies also at the interface of the elastic layer. Table 2 also

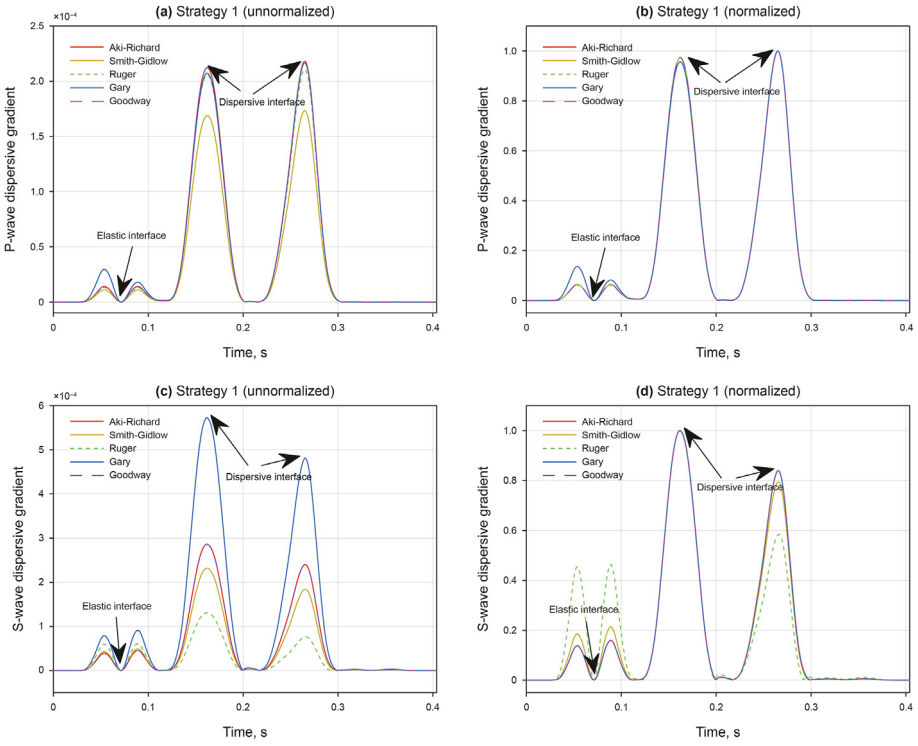

Fig. 6. Comparison of inversion results calculated using strategy 1 based on different approximate Zoeppritz approximations. (a and b) Unnormalized and normalized P-wave dispersion gradients; (c and d) Unnormalized and normalized S-wave dispersion gradients.

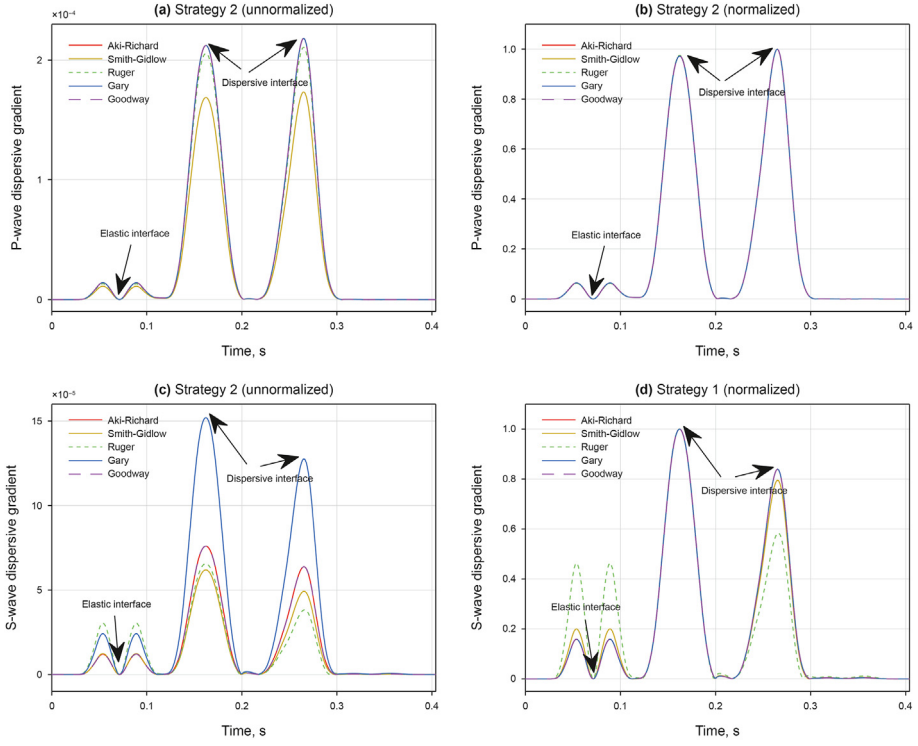

Fig. 7. Comparison of inversion results calculated using strategy 2 based on different approximate Zoeppritz approximations. (a and b) Unnormalized and normalized P-wave dispersion gradients; (c and d) Unnormalized and normalized S-wave dispersion gradients.

suggests that the indicating ability factor in this case is extremely small ($\zeta_S = 1.26$). It means that S-wave dispersion gradient obtained by the Rüger equation is not effective at indicating the presence of reservoirs compared to the other Zoeppritz approximations. In addition, Figs. 6 and 7 reveal that the dispersion gradients based on strategies 1 and 2 are largely consistent after

Table 2
Indicating ability factors for strategies 1 and 2 based on different Zoeppritz approximations.

		Aki-Richard	Smith-Gidlow	Ruger	Gary	Goodway
ζ_P	Strategy 1	15.05	15.17	15.65	6.97	15.05
	Strategy 2	15.05	15.17	15.65	15.05	15.05
ζ_S	Strategy 1	5.27	3.73	1.26	5.27	5.27
	Strategy 2	5.27	3.97	1.26	5.27	5.27

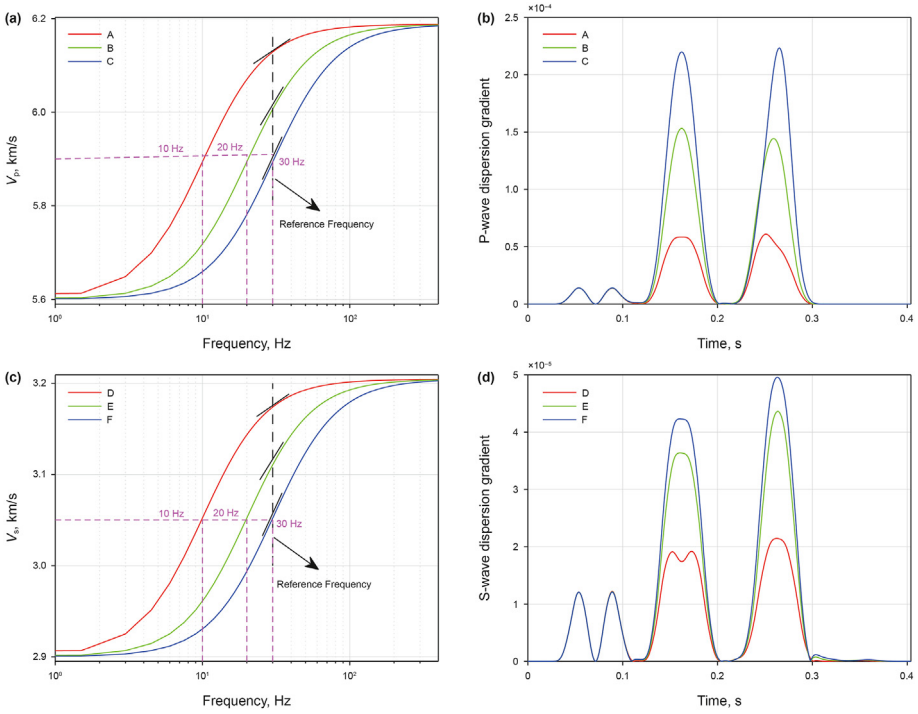

Fig. 8. The influence of velocity dispersions with different characteristic frequencies. A–C: Dispersive P-wave velocity and constant S-wave velocity of 3.04 km s^{-1}. D–F: Dispersive S-wave velocity and constant P-wave velocity of 5.91 km s^{-1}. The short black lines approximate the slope of the curve at the reference frequency.

normalization. The indicating ability factors obtained by strategy 1 and strategy 2 are also very similar, except the Gary equation (see Table 2) in which case $\zeta_P = 6.97$ for Strategy 1 and $\zeta_P = 15.05$ for Strategy 2. However, by examining the dispersion gradients for the Gary equation shown in Fig. 6b, we think this difference is acceptable. These results indicate that when the velocity is not available, it is still feasible to use strategy 2 to obtain reliable dispersion attributes. In fact, because it does not require velocity information, strategy 2 is much simpler to apply, and has advantages in practical applications compared with strategy 1. Based on the above analysis, the Goodway approximation based on strategy 2 will be used to perform the FAVO inversion in the following tests.

3.2. P- and S-wave velocity dispersion

Next, we analyze the influence of the velocity dispersion on FAVO results. Firstly, we investigate the effects of velocity dispersions with different characteristic frequencies using several numerical experiments (A, B, …, F). For experiments A-C, the S-wave velocities are frequency-independent and equal to 3.04 km s^{-1},

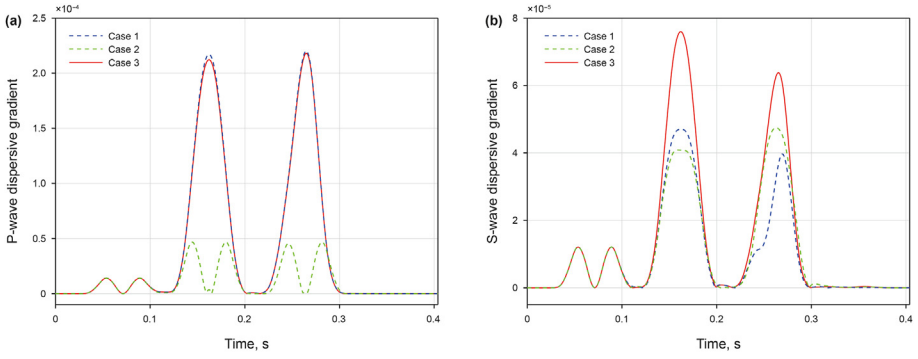

Fig. 9. Dispersion gradients for (a) P- and (b) S-waves. Case 1: only P-wave velocity is dispersive; Case 2: only S-wave velocity is dispersive; Case 3: both velocities are dispersive.

Table 3
Indicating ability factors for the three cases shown in Fig. 9

	P-wave velocity (Case 1)	S-wave velocity (Case 2)	P- and S-wave velocities (Case 3)
ζ_P	15.40	3.32	15.05
ζ_S	3.27	3.37	5.27

while the P-wave velocities are dispersive with different characteristic frequencies and vary with the frequency in the same way (see Fig. 8a). In contrast, for experiments D-F, the P-wave velocities are constant (5.91 km s^{-1}) but the S-wave velocities are frequency-dependent (see Fig. 8c). The corresponding inversion results for all cases are shown in Fig. 8. As can be seen, the inverted dispersion gradients increase with increasing slope of the velocity dispersion at the reference frequency, which indicates that the inversion results obtained by FAVO technique can only reflect the slope of the velocity dispersion (or the dispersion gradient) at the reference frequency. This can also be inferred from the FAVO inversion theory. The Taylor expansion of the Zoeppritz approximations at the reference frequency in the theory has already determined that the FAVO inversion results can only reflect the velocity dispersion at the reference frequency.

Then, we examine whether the FAVO method could invert the pure P-wave and S-wave dispersions from the seismic records. Three cases are considered here: (1) only the P-wave velocity in the dispersive layer is dispersive, and the S-wave velocity is 3.04 km s^{-1}, (2) only the S-wave velocity is dispersive, and the P-wave velocity is 5.91 km s^{-1}, and (3) both P- and S- wave velocities are dispersive (see Fig. 2).

Fig. 9 shows the inversion results of P- and S-wave dispersion gradients in the three cases, and Table 3 provides the corresponding indicating ability factors. For the P-wave dispersion gradient, significant anomalies occur at the dispersive interfaces in cases whenever P-wave velocity is dispersive, while the S-wave velocity dispersion has much less contribution to the P-wave dispersion gradient. We can also observe from Table 3 that the P-wave indicating ability factors are around 15 in Case 1 and Case 3, but only 3.32 in Case 2. In contrast, the inversion results for the S-wave dispersion gradient demonstrate obvious anomalies in all three cases. In particular, for case 1 in which only P-wave velocity dispersion exists, the S-wave dispersion anomaly is also unexpectedly significant with an indicating ability factor of 3.27. Note that the indicating ability factor in Case 3 (where only the S-wave velocity is dispersive) is only 3.37. This phenomenon may have been caused by the linear coupling between P- and S-wave dispersion terms during the inversion, which implies that it is difficult to obtain pure S-wave dispersion attributes using FAVO inversion based on PP reflection seismic data. In other words, although one can obtain the dispersion attributes of P- and S-waves using PP reflection angle gathers, FAVO inversion delivers a much lower accuracy for the S-wave dispersion than that of the P-wave dispersion due to the coupling effect of P- and S-wave dispersion terms. The obtained dispersion of S-wave may be caused by either the coupling effect or by the actual S-wave dispersion of the medium, which as a result makes it difficult to identify the origin of the dispersion. In addition, Table 3 illustrates that the indicating ability of the S-wave dispersion gradient is much weaker than that of the P wave. Therefore, when PP reflection seismic data is utilized for reservoir prediction and fluid identification, the P-wave dispersion gradient appears to be more suitable than the S-wave dispersion gradient as a fluid indicator for hydrocarbon detection.

3.3. Inversion input data

For practical applications, researchers often focus more on P-wave dispersion. To obtain the P-wave dispersion attributes, either post-stack seismic records (self-excitation and self-gathering) or pre-stack angle gathers are generally used in the FAVO inversion. This section compares the inversion results of the dispersion gradients obtained using these two kinds of synthetic seismic data as inversion inputs.

Fig. 10 presents the dispersion gradient results calculated based on post-stack data and pre-stack angle gathers (5–40°, with an angular interval of 5°) respectively. We can see that when the post-stack gathers are used as the input data, only the P-wave dispersion gradient could be obtained. In addition, the results of the P-wave dispersion gradient acquired using the two kinds of synthetic data are almost identical, with a high P-wave indicating ability factor of 10.83 and 16.38 respectively. This indicates that, in practical applications, we can invert the P-wave dispersion gradient directly from the post-stack seismic data. In fact, the actual post-stack seismic data generally has a higher signal-to-noise ratio than the pre-stack angle gather data, and hence is more beneficial to the accurate inversion of the P-wave dispersion. Therefore, if only the P-wave dispersion information is desired, post-stack data can meet the principal requirements. On the other hand, the main purpose of using angle gathers as the inversion input is to obtain the S-wave dispersion. However, the analysis presented in Section 3.2 has demonstrated the difficulty of obtaining pure S-wave dispersion based on PP reflection seismic data.

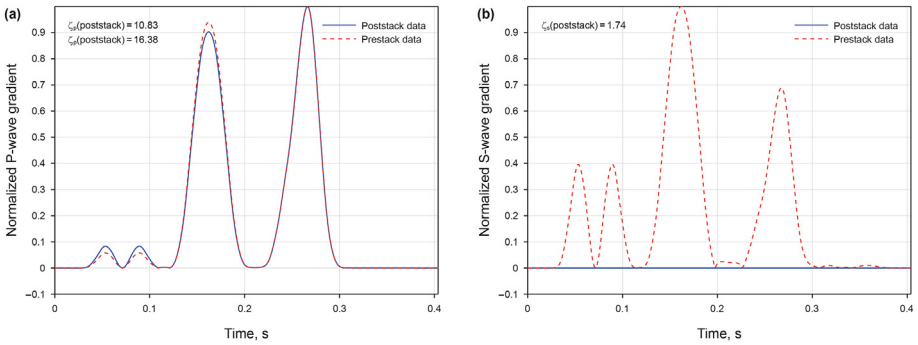

Fig. 10. (a) P- and (b) S-wave dispersion gradients calculated using the synthetic post-stack seismic data and angle gathers. ζ_P, ζ_S are the indicating ability factors for the P- and S-wave dispersion gradients.

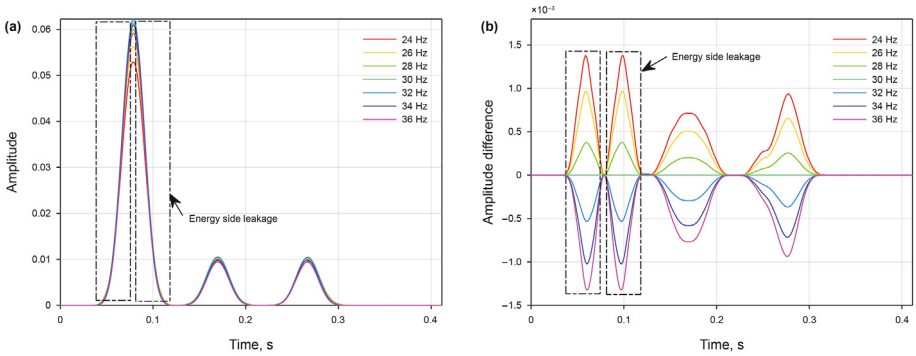

Fig. 11. Energy side leakage phenomenon in presence of a strong reflection elastic interface: (a) balanced time-frequency spectrum; (b) spectrum difference, which denotes the deviation between the amplitudes at dominant frequency and at other frequencies.

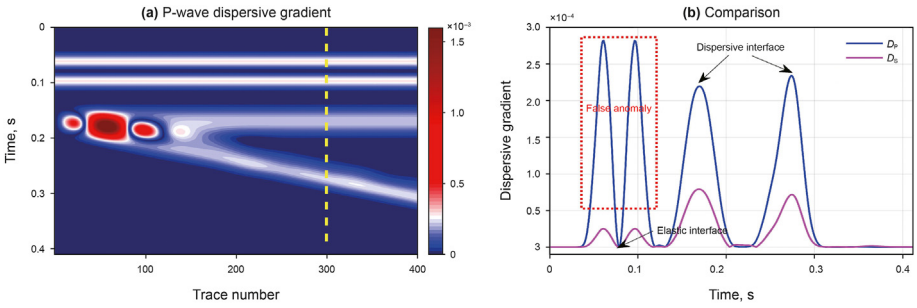

Fig. 12. Dispersion gradient obtained by FAVO inversion in presence of a strong reflection elastic interface.

3.4. Elastic strong reflection interface

To discuss the influence of the elastic strong reflection interface on the FAVO inversion, we modify the model parameters of the first elastic layer as $V_P = 5.0$ km/s, $V_S = 2.8$ km/s, and $\rho = 2.5$ g/cm^3, so that the first interface is converted into a strongly reflective interface. Due to the spectrum decomposition technology used, it is generally difficult to normalize the amplitude at each frequency near the elastic interface into a completely consistent state after the spectrum balance. Therefore, the amplitude inconsistency is inevitable near the peak of the spectrum at the elastic interface (see black dotted frames in Fig. 11a), though it can be more or less significant. We call this phenomenon "energy side leakage." For a general elastic interface, the effect of the energy side leakage is often negligible, so its influence can be ignored. However, for strong reflection interface, the order of magnitude of the energy side leakage will likely be equal to or even larger than the desired dispersion gradient (as shown in Fig. 11b), and thus cannot be ignored.

Fig. 12 presents the inversion results in presence of a strong reflection elastic interface. As shown in Fig. 12a, apparent anomalies occur at the dispersive interfaces and also on both sides of the strong reflection interface. Fig. 12b shows that the anomalies near the elastic interface are especially evident (see those encircled by the red dotted frame). This "false" P-wave dispersion is even higher than the actual P-wave dispersion at the dispersive interface. Such a phenomenon could cause a confusion between the strong non-reservoir interface and the actual reservoir in the real application of FAVO inversion to seismic field data, and further increase the difficulty of reservoir prediction and fluid discrimination. It could even lead to a completely wrong conclusion. In contrast, the S-wave dispersion gradient here shows a relatively slight reaction to the elastic interface due to the much weaker S-wave impedance contrast. To circumvent the negative effects of energy side leakage, we can identify and eliminate the strong reflection non-reservoir interface before FAVO inversion with the help of well logging and geological data. From Fig. 12, we can also see that large dispersion anomalies also appear in the thinner wedge-shaped region. This is caused by the tuning effect of the thin layers. Therefore, the influences of thin layers should also be carefully considered during the FAVO inversion.

3.5. The influence of noise

To further investigate the influence of noise on the inversion results, different levels of Gaussian random noise (i.e., 3%, 5%, 10%, 15%, which denote the ratio of noise energy to signal energy) are added to Fig. 3b to generate noisy angle gathers, as shown in Fig. 13. The quality of the angle gathers becomes worse with increased noise, and when the noise level is higher than 5%, some useful information in the angle gathers is smeared.

Fig. 14 shows the inverted P- and S-wave dispersion gradients by FAVO inversion from the noisy angle gathers with different levels of Gaussian random noise. Table 4 lists the corresponding indicating ability factors. It is shown that with increases in noise level, the indicating ability of the P- and S-wave dispersion gradients is weakened. Nevertheless, Fig. 14 illustrates that the P-wave indicating ability factor is still within an acceptable range even in the case of 15% noise. For this case, the P-wave indicating ability factor is 12.4. Compared with the P-wave gradient, the S-wave dispersion gradient has a much weaker indicating capability at all noise levels and its maximum indicating ability factor is only 5.27.

3.6. Comparison with iso-frequency anomalies

To compare the dispersion gradient attributes with the iso-

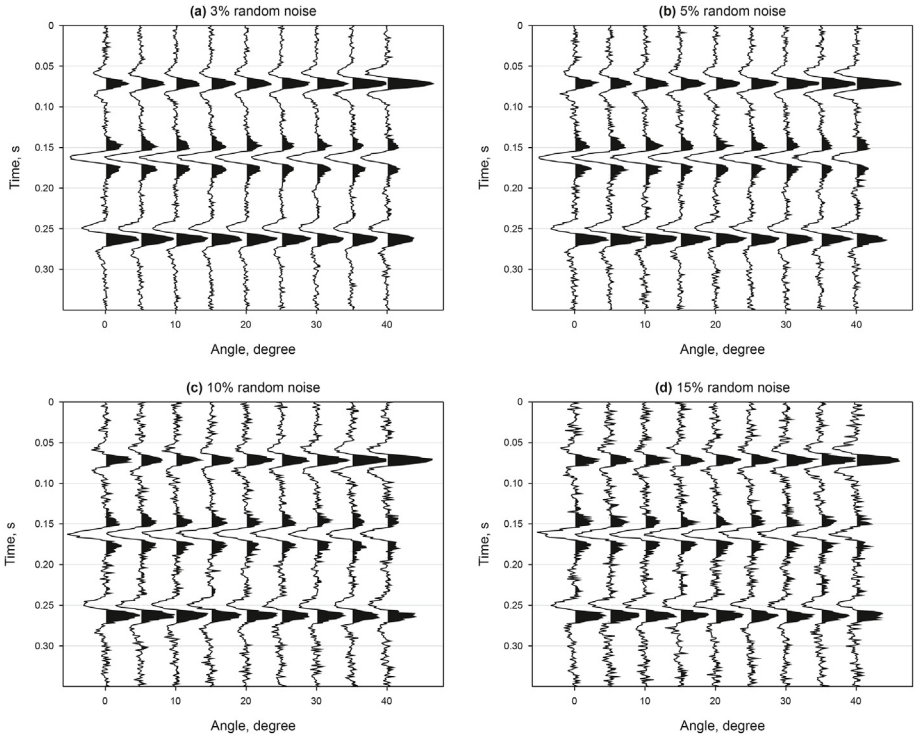

Fig. 13. The angle gathers at Trace 300 with (a) 3%, (b) 5%, (c) 10%, and (d) 15% Gaussian random noise.

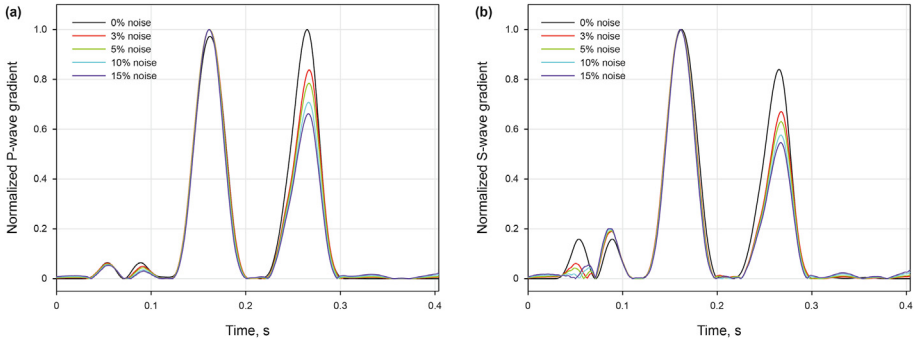

Fig. 14. The normalized (a) P- and (b) S-wave dispersion gradients obtained by FAVO inversion with different levels of Gaussian random noise.

Table 4
Indicating ability factors for the cases with different Gaussian random noise.

Noise	0%	3%	5%	10%	15%
ζ_P	15.05	13.40	13.13	12.73	12.40
ζ_S	5.27	3.53	3.29	2.93	2.71

frequency anomalies, we also calculate iso-frequency data using the SPWVD spectral decomposition technique. Fig. 15 presents the iso-frequency sections (15 Hz, 25 Hz and 35 Hz) obtained from the synthetic seismic data with different incident angles for the wedge-layered model. We can see that for all the incident angles, strong energy appears at both the top and bottom of the dispersive layer at a low frequency of 15 Hz, and then gradually decreases with increasing frequency. In contrast, the energy at the elastic interface shows no frequency dependency, and only varies with the angle of incidence due to the effect of amplitude versus angle. For the wedge-layered model considered, the amplitude of the seismic data increases with the incident angle (see Fig. 3b) and thus exhibits a strong energy at 30° for all frequencies. Fig. 15 illustrates that although the iso-frequency anomaly can indicate the gas reservoir, it may also indicate some other non-reservoir bodies with strong energies, such as the elastic interface in this example. Therefore, the iso-frequency anomaly is not the best choice for hydrocarbon detection.

In contrast, the inverted dispersion gradient attributes using the FAVO technique have higher resolution because it removes the band-pass filter effect of the wavelet (see Fig. 16a and b). The dispersion gradients at the elastic interface are rather small compared with those at the dispersive interfaces, and thus can indicate the reservoir more accurately. In addition, the P-wave dispersion gradient shows better indicating ability than the S-wave dispersion gradient. From Fig. 16, we can also observe that there are significant tuning effects in both elastic and dispersive cases when the thickness of the wedge-shaped interlayer is < 100 m. With

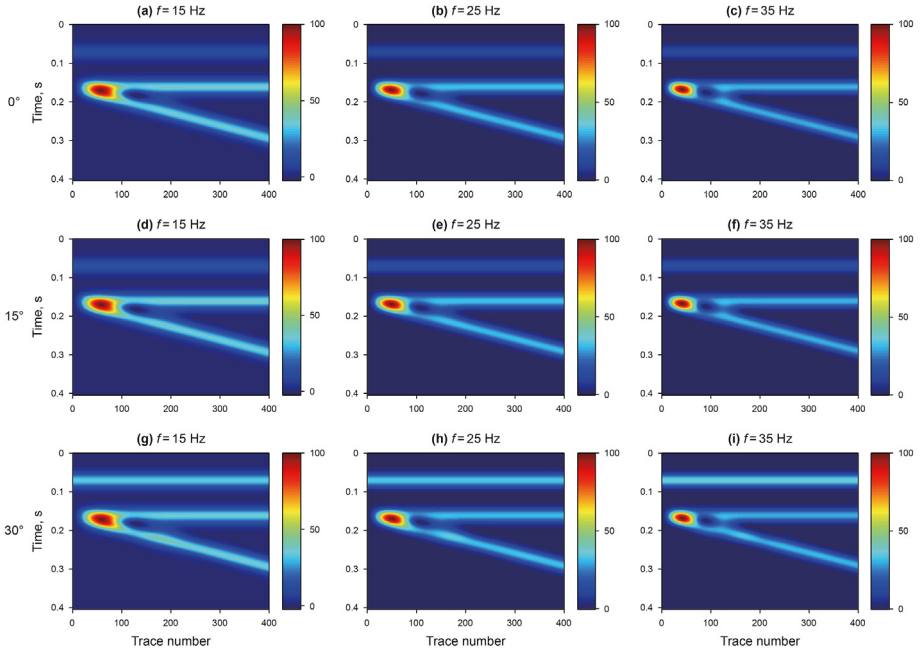

Fig. 15. Iso-frequency sections for the wedge-layered model: (a–c) 15 Hz, 25 Hz, and 35 Hz sections with an incident angle of 0° (corresponding to the post-stack case), and the iso-frequency sections with an incident angle of (d–f) 15° and (g–i) 30° (corresponding to the pre-stack case).

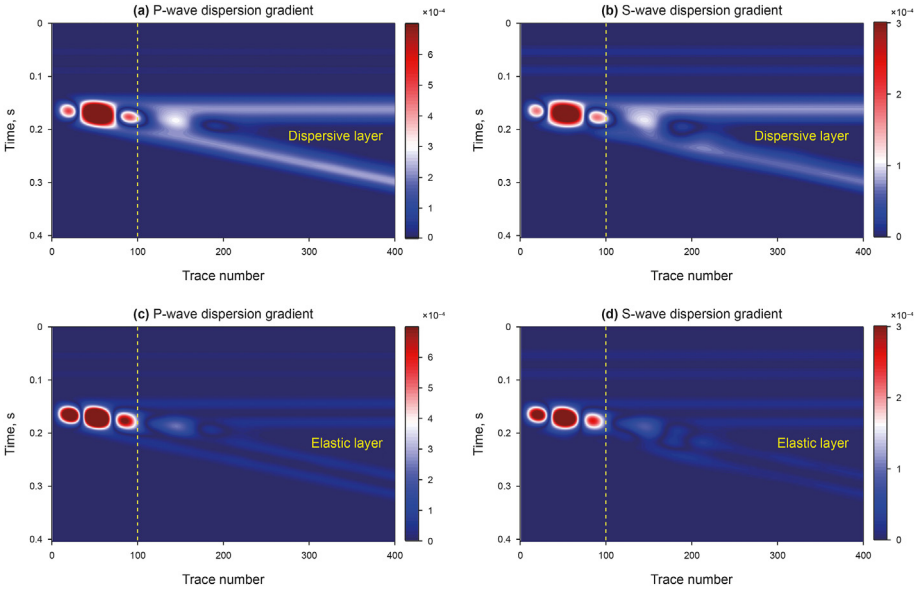

Fig. 16. The P- and S-wave dispersion gradients obtained by FAVO inversion for the dispersive (a, b) and elastic (c, d) wedge-layered model. Significant tuning effects can be observed in both the elastic and dispersive cases when the thickness of the wedge-shaped interlayer is less than 100 m.

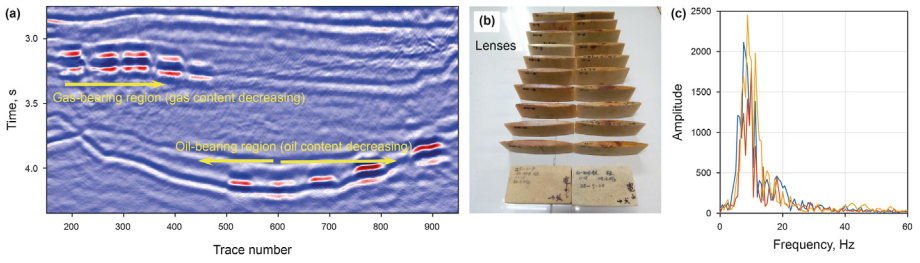

Fig. 17. Seismic physical model. (a) Post-stack seismic profile, (b) lenses in the physical model, and (c) spectrum of the seismograms.

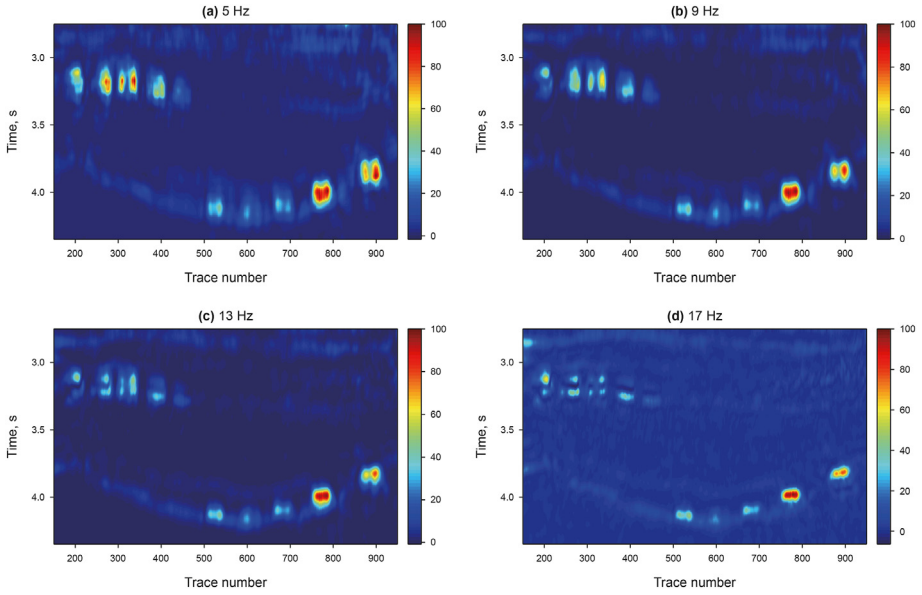

Fig. 18. Iso-frequency sections obtained from the post-stack data of the seismic physical model: (a) 5 Hz, (b) 9 Hz, (c) 13 Hz and (d) 17 Hz.

further increase in thickness, the tuning effects weaken and then disappear. This suggests that the dispersion gradients obtained by FAVO inversion have difficulties in indicating hydrocarbon reservoirs with small thicknesses. Therefore, both the iso-frequency method and the FAVO technique suffer from thin bed tuning effects. In this case, logging, geological, and other relevant data should be integrated with the dispersion gradients to help distinguish whether the anomalies are caused by thin hydrocarbon reservoirs or other non-reservoir bodies.

4. Practical applications

This section presents the application of FAVO inversion to actual seismic data. The Goodway approximation and SPWVD spectral decomposition technique are employed.

4.1. Seismic physical model

The seismic physical model used here consists of two regions: a gas-bearing region and an oil-bearing region. The gas-bearing region consists of lenses containing gas-water mixtures with different gas content, while the oil-bearing region comprises of oil-saturated lenses with different porosities (as shown in Fig. 17b). The physical model and the lenses are composed of quartz sand and cemented mixtures (such as epoxy resin, silicone rubber, and curing agent). The length, width, and thickness of each lens are 10 cm × 5 cm × 1 cm, respectively. During the seismic physical simulation, the physical model is placed in water, and the source and geophone are excited and received on the water surface. Fig. 17a displays the post-stack seismic section of the seismic physical model. The spectrum analysis of the received seismic records reveals that the dominant frequency of the signal is about 10 Hz with a frequency band of 0–40 Hz (see Fig. 17c).

Fig. 18 shows the iso-frequency sections (5 Hz, 9 Hz, 13 Hz, and 17 Hz) obtained from the post-stack seismic data of the physical model. We can observe that the energy in both the gas-bearing and oil-bearing regions is strong at low frequencies, but decreases rapidly with increased frequency, especially in the gas-bearing region. In addition, no obvious low-frequency shadow phenomena are observed for the physical model, probably due to the narrow frequency band of the seismic data and the simple structure of the physical model.

In the FAVO inversion, the dominant frequency of the signal is taken as the reference frequency, and the SPWVD technique with a time window of 0.09 s is applied to perform the spectral decomposition. The maximum amplitude within 2.8–2.9 s denotes the location of the elastic interface and is used to calculate the weighted spectrum balance coefficient. To prevent energy side leakage and obtain accurate P-wave dispersion, the strong reflection interface between the solid model and water was eliminated, and only the effective post-stack data for the solid model area are retained (Fig. 17a). Fig. 19 shows the time-frequency spectra of the post-stack seismic data before and after the spectrum balance recorded at Trace 270. It can be observed that the reflection amplitudes at all frequencies are almost consistent after spectrum balance, except for those at the time interval 3–3.4 s (i.e., the gas-bearing region).

Fig. 20 presents the P-wave dispersion gradient attribute section estimated by FAVO inversion for the physical model. As can be seen, obvious dispersion anomalies occur in both the gas-bearing and oil-bearing regions, and the P-wave dispersion gradient also exhibits an obvious change with the gas content. At an intermediate gas content, the dispersion is the highest, and while the gas content further decreases or increases, the dispersion becomes weaker. This result has a good agreement with the White's partial saturation theory (White et al., 1976). It can also be observed from Fig. 20 that when the oil content is high, the indicating ability of the dispersion gradient becomes much weaker. This indicates that it is more difficult for the dispersion gradient to detect a reservoir with a high oil saturation compared with a gas-bearing reservoir. In addition, since the lenses are very thin, the P-wave dispersion attribute could not clearly depict the boundary of the lenses. Instead, it could only reflect their general location. Nevertheless, the FAVO inversion based on the SPWVD technique and Goodway approximation generally performs well in hydrocarbon detection.

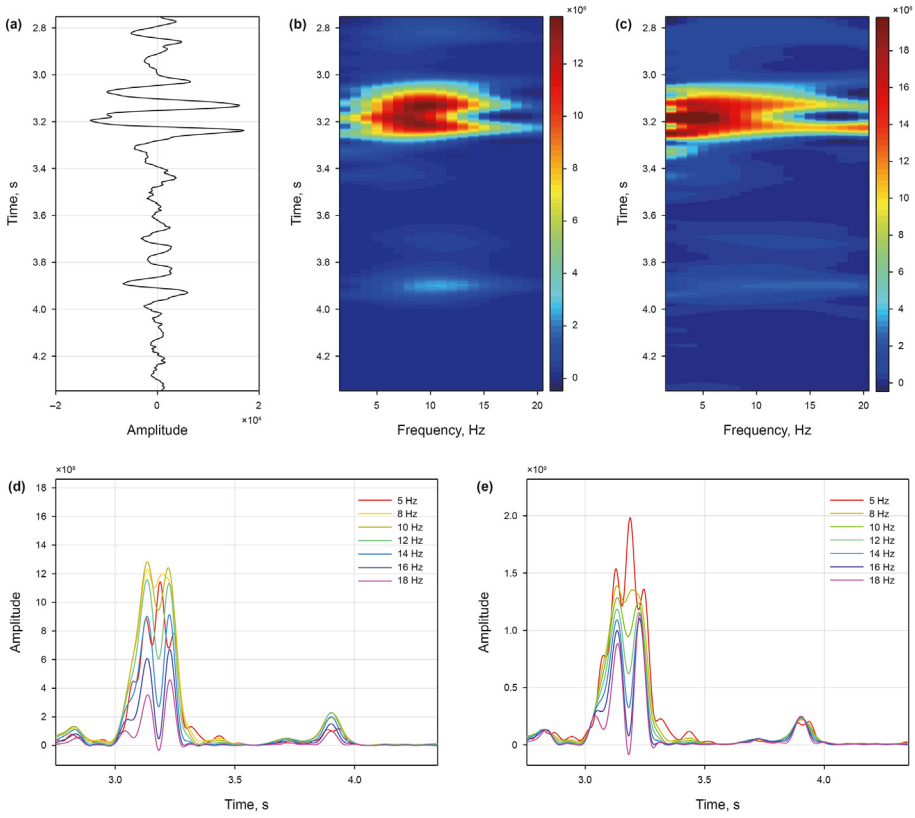

Fig. 19. The results of spectral decomposition for Trace 270: (a) the original seismogram, and the time-frequency spectra of the seismogram (b, d) before and (c, e) after spectrum balance.

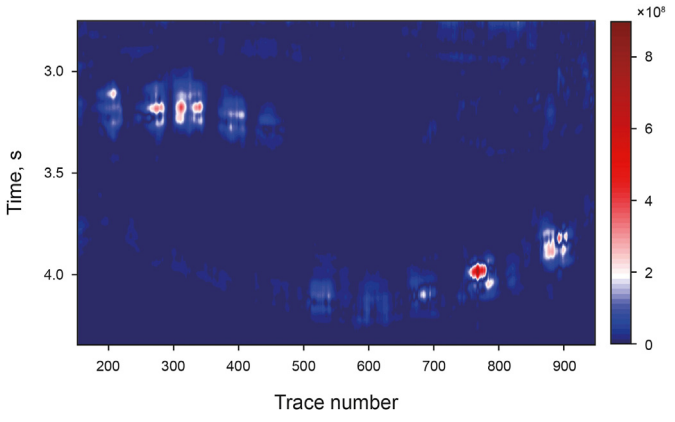

Fig. 20. P-wave dispersion gradient calculated using the post-stack data of the seismic physical model.

4.2. Tight sandstone reservoir

We further apply the FAVO inversion in detecting a real gas-bearing tight sandstone reservoir, the post-stack seismic section of which is shown in Fig. 21. Three post-stack seismic traces are randomly selected to determine the dominant frequency of the seismic data. A Fourier transform is performed to obtain the frequency-domain spectrum shown in Fig. 21b. As can be seen, the dominant frequency of the tight sandstone seismic data is about 24 Hz, and the effective frequency band is 0–60 Hz. Therefore, 24 Hz is chosen as the reference frequency for the FAVO inversion.

In addition, the well-seismic calibration and gas tests suggest that the total gas production of well W1 is approximately 37.5×10^4 m^3, with the corresponding gas-bearing interval on the seismic profile being 1.67–1.68 s, and the total gas production of well W2 is about 48.0×10^4 m^3, with the corresponding gas-bearing interval on the seismic profile being 1.68–1.69 s. The total gas production of well W3 is 10.8×10^4 m^3 and the corresponding gas-bearing location on the seismic profile is at 1.68 s.

Fig. 22 shows the P-wave dispersion attributes for the gas-bearing tight sandstone reservoir. It can be seen that the P-wave dispersion exhibits obvious anomalies near the gas-bearing positions of the three wells. For W1 and W2, the peak value of the P-wave dispersion corresponds to their respective gas-bearing position. For well W3, the P-wave dispersion exhibits a relative lower anomaly at the gas-bearing location. Fig. 23 compares the total gas production and the P-wave dispersion at the gas-bearing locations of these three wells. As can be seen, W1 and W2 are high-production wells, while W3 has a relatively lower production. In addition, the P-wave dispersion at the gas-bearing positions of the three wells is positively correlated with the total gas production. It indicates that the P-wave dispersion can not only indicate the location of the gas reservoir, but can also reflect said reservoir's physical properties to a certain extent.

To further demonstrate the indicating ability of the dispersion gradient, we compare it with four commonly-used conventional seismic attributes, including the Russell fluid factor, AVO gradient attribute, AVO intercept attribute, and shear modulus (as shown in Fig. 24). As can be seen, high values of the Russell fluid factor and AVO gradient appear above the gas-bearing reservoir, and no anomalies are observed in the target hydrocarbon accumulation.

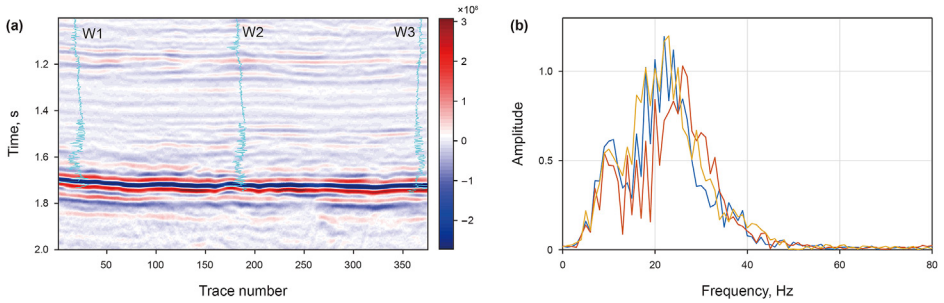

Fig. 21. (a) Post-stack seismic section and (b) spectrum of hydrocarbon-bearing tight sandstone reservoir.

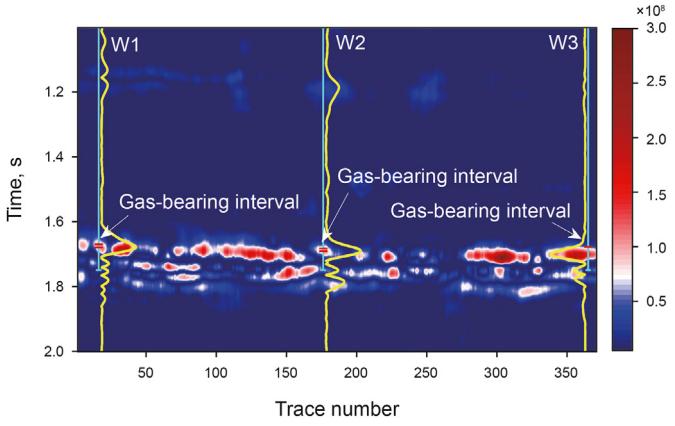

Fig. 22. P-wave dispersion for the gas-bearing tight sandstone reservoir. The yellow lines denote the curves of the P-wave dispersion gradient at the location of the wells.

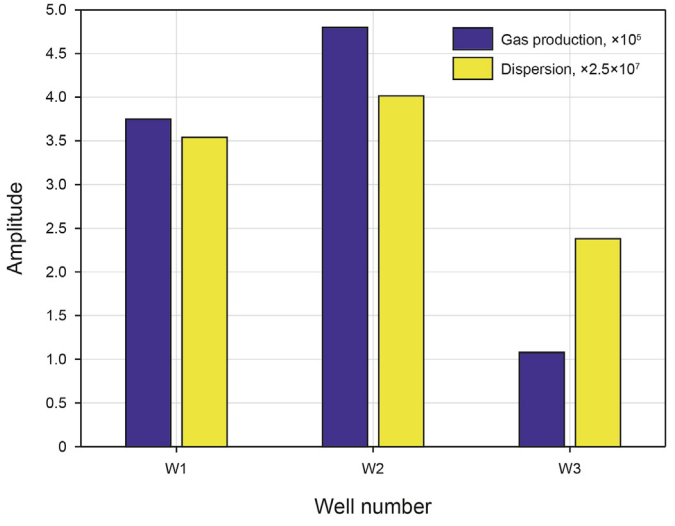

Fig. 23. Total gas production for three wells and the corresponding P-wave dispersion at gas-bearing positions.

This suggests that the Russell fluid factor and AVO gradient are not good hydrocarbon indicators in this context. In contrast, the AVO intercept and shear modulus have better indicating abilities. Obviously, anomalous values of the AVO intercept and shear modulus are observed around the hydrocarbon reservoir. However, one can also see significant anomalies caused by non-reservoir interfaces, which as a result blurs the useful fluid information. In comparison with conventional attributes, the dispersion gradient given in Fig. 22 has a much higher resolution and is less susceptible to the impacts of non-reservoir bodies. Overall, these results demonstrate that the dispersion gradient attribute obtained by FAVO inversion has a better fluid indicating ability for hydrocarbon detection, compared to the conventional seismic attributes.

5. Conclusions

We have proposed a unified equation for FAVO inversion by combining several classical Zoeppritz approximation equations, as well as two inversion strategies. Based on a theoretical model, the influences of various factors on the FAVO inversion are analyzed, such as the selection of the Zoeppritz approximation, the degree of velocity dispersion, the selection of inversion input data, and the effects of a strong elastic reflection interface. The results show that: (1) the Aki-Richard, Smith-Gidlow, and Goodway approximations deliver similar inversion results, while the Gary equation shows a slightly different trend around the elastic layer. However, all these approximations have a better performance than the Rüger equation. (2) The inversion accuracies of strategies 1 and 2 are generally similar, which implies that even if the velocity information is not available, one can still obtain accurate dispersion attributes using strategy 2. (3) For FAVO inversion based on PP reflection seismic data, the P-wave dispersion gradient is found to be more suitable than the S-wave dispersion gradient as a hydrocarbon indicator. (4) If only the P-wave dispersion attribute is desired, using either post-stack data or pre-stack angle gathers as input data have little effect on the inversion results. (5) A strong reflection interface will lead to energy side leakage in FAVO inversion, which may cause a significant "false" P-wave dispersion that poses difficulty on differentiating reservoir and non-reservoir regions. The negative effects of this phenomenon can be prevented by eliminating the strong reflection interface with the help of logging and geological data. (6) The tuning effects of thin layers should also be accounted in FAVO inversion. In addition, we also verify the reliability and practicability of the FAVO technique by applying it to a seismic physical model and the seismic field data. The application examples demonstrate that the dispersion attributes obtained with FAVO inversion have higher resolution for hydrocarbon detection compared to the commonly-used seismic attributes. Moreover, the dispersion attributes could not only indicate the location of a hydrocarbon reservoir, but could also reflect its physical properties to a certain extent. However, to diminish the ambiguity of reservoir characterization and improve the reliability of the inversion results in real applications, FAVO inversion must be integrated with the drilling and geological information.

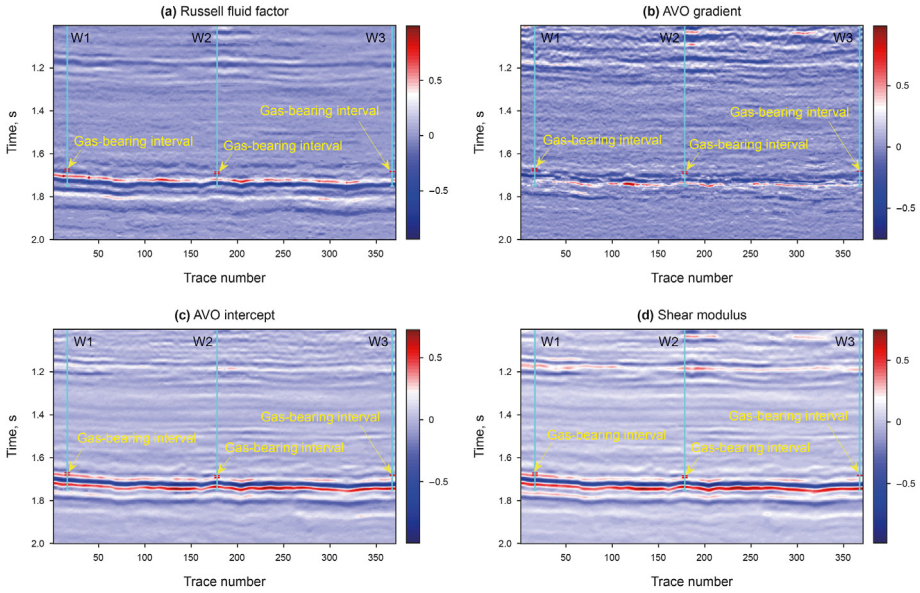

Fig. 24. The normalized results of conventional seismic attributes for the gas-bearing tight sandstone reservoir: (a) Russell fluid factor, (b) AVO gradient, (c) AVO intercept, and (d) shear modulus.

Declaration of competing interest

The authors declare that they have no known competing financial interests or personal relationships that could have appeared to influence the work reported in this paper.

Acknowledgements

This work is supported by the National Natural Science Foundation of China (42304141, 41574103 and 41974120) and the Joint Funds of the National Natural Science Foundation of China (U20B2015).

References

Ajaz, M., Ouyang, F., Wang, G.H., Liu, S.L., Wang, L.X., Zhao, J.G., 2021. Fluid identification and effective fracture prediction based on frequency-dependent AVOAz inversion for fractured reservoirs. Petrol. Sci. 18 (4), 1069–1085. https://doi.org/10.1016/j.petsci.2021.07.011.

Aki, K., Richards, P., 2009. Quantitative Seismology. University Science Books. Society of Exploration Geophysicists, America.

Avseth, P., Mukerji, T., Jørstad, A., Mavko, G., Veggeland, T., 2001. Seismic reservoir mapping from 3-D AVO in a North Sea turbidite system. Geophysics 66 (4), 1157–1176. https://doi.org/10.1190/1.1487063.

Batzle, M.L., Han, D.H., Hofmann, R., 2006. Fluid mobility and frequency-dependent seismic velocity-Direct measurements. Geophysics 71 (1), N1–N9. https://doi.org/10.1190/1.2159053.

Castagna, J.P., Swan, H.W., Foster, D.J., 1998. Framework for AVO gradient and intercept interpretation. Geophysics 63 (3), 948–956. https://doi.org/10.1190/1.1444406.

Castagna, J., Sun, S., Siegfried, R., 2003. Instantaneous spectral analysis: detection of low-frequency shadows associated with hydrocarbons. Lead. Edge 22 (3), 120–127. https://doi.org/10.1190/1.1559038.

Chapman, M., Liu, E., Li, X., 2006. The influence of fluid-sensitive dispersion and attenuation on AVO analysis. Geophys. J. Int. 167 (1), 89–105. https://doi.org/10.1111/j.1365–246X.2006.02919.x.

Chen, H.Z., 2020. Seismic frequency component inversion for elastic parameters and maximum inverse quality factor driven by attenuating rock physics models. Surv. Geophys. 41 (2), 835–857. https://doi.org/10.1007/s10712-020-09593-6.

Chen, H.Z., Moradi, S., Innanen, K.A., 2021. Joint inversion of frequency components of PP and PSV-wave amplitudes for attenuation factors using second-order derivatives of anelastic impedance. Surv. Geophys. 42 (1), 1–27. https://doi.org/10.1007/s10712-021-09649-1.

Chen, H.Z., Yin, X.Y., Gao, J.H., et al., 2015. Seismic inversion for underground fractures detection based on effective anisotropy and fluid substitution. Sci. China Earth Sci. 58, 805–814. https://doi.org/10.1007/s11430-014-5022-1.

Chen, X.H., He, Z.H., Huang, D.J., et al., 2009. Low frequency shadow detection of gas reservoirs in time-frequency domain. Chin. J. Geophys. 52 (1), 215–221. https://doi.org/10.1016/j.jappgeo.2016.05.010 (in Chinese).

Chen, X., Qi, Y., He, X., et al., 2016a. Phase-shifted based numerical method for modeling frequency-dependent effects on seismic reflections. Pure Appl. Geophys. 173 (8), 2899–2912. https://doi.org/10.1007/s00024-016-1290-3.

Chen, X., Zhong, W., Gao, G., et al., 2016b. Numerical analysis of velocity dispersion in multi-phase fluid-saturated porous rocks. Pure Appl. Geophys. 174 (3), 1–17. https://doi.org/10.1007/s00024-016-1457-y.

Cheng, B.J., Xu, T.J., Li, S.G., 2012. Research and application of frequency dependent AVO analysis for gas recognition. Chin. J. Geophys. 55 (2), 608–613. https://doi.org/10.6038/j.issn.0001-5733.2012.02.023 (in Chinese).

Ebrom, D., 2004. The low-frequency gas shadow on seismic sections. Lead. Edge 23 (8), 772–773. https://doi.org/10.1190/1.1786898.

Goloshubin, G., Schuyver, C.V., Korneev, V., et al., 2006. Reservoir imaging using low frequencies of seismic reflections. Lead. Edge 25, 527–531. https://doi.org/10.1190/1.2202652.

Goodway, B., 1997. Improved AVO fluid detection and lithology discrimination using Lamé petrophysical parameters, 'λρ', 'μρ', & 'λ/μ' fluid stack, from P and S inversions. SEG Tech. Progr. Expand. Abstr. 183–186. https://doi.org/10.1190/1.1885795.

Gray, D., Goodway, B., Chen, T., 1999. Bridging the gap: using AVO to detect changes in fundamental elastic constants. SEG Tech. Progr. Expand. Abstr. 2061–2064. https://doi.org/10.1190/1.1821163.

Guo, Z.Q., Liu, C., Li, X.Y., et al., 2016. Modeling and analysis of frequency-dependent AVO responses in inelastic stratified media. Chin. J. Geophys. 59 (2), 664–672. https://doi.org/10.6038/cjg20160223 (in Chinese).

Guo, Z., Liu, C., Li, X., et al., 2015. An improved method for the modeling of frequency-dependent amplitude-versus-offset variations. IEEE Geosci. Remote S. 12 (1), 63–67. https://doi.org/10.1109/LGRS.2014.2326157.

Huang, G.T., Li, J.Y., Chen, X.H., et al., 2017. Frequency-dependent AVO reservoir identification method based on sparse constrained inversion spectral decomposition. Chin. J. Geophys. 60 (10), 3984–3994. https://doi.org/10.6038/cjg20171025 (in Chinese).

Korneev, V., Goloshubin, G., Daley, T., Silin, D., 2004. Seismic low-frequency effects in monitoring fluid-saturated reservoirs. Geophysics 69 (2). https://doi.org/10.1190/1.1707072, 522–332.

Kumar, D., Zhao, Z., Foster, D.J., Danica, D., Sen, M.K., 2019. Frequency-dependent AVO analysis using the scattering response of a layered reservoir. Geophysics 85 (2), N1–N16. https://doi.org/10.1190/geo2019-0167.1.

Liu, H., Li, J., Chen, X., et al., 2016. Amplitude variation with offset inversion using the reflectivity method. Geophysics 81 (4), R185–R195. https://doi.org/10.1190/GEO2015-0332.1.

Liu, J., He, Z.L., Liu, X.W., Huo, Z.Z., Peng, G., 2019. Using frequency-dependent AVO inversion to predict the "sweet spots" of shale gas reservoirs. Mar. Petrol. Geol. 102, 283–291.

Liu, W., Cao, S., Jin, Z., Wang, Z., Chen, Y., 2018. A novel hydrocarbon detection approach via high-resolution frequency-dependent AVO inversion based on variational mode decomposition. IEEE Trans. Geosci. Rem. Sens. 56 (4), 2007–2024. https://doi.org/10.1109/TGRS.2017.2772037.

Ludmila, A., Batzle, M., 2008. Elastic properties of carbonates from laboratory measurements at seismic and ultrasonic frequencies. Lead. Edge 27 (8),

1026–1032. https://doi.org/10.1190/1.2967556.
Odebeatu, E., Zhang, J., Chapman, M., et al., 2006. Application of spectral decomposition to detection of dispersion anomalies associated with gas saturation. Lead. Edge 25 (2), 206–210. https://doi.org/10.1190/1.2172314.
Ostrander, W., 1984. Plane-wave reflection coefficients for gas sands at non-normal incidence. Geophysics 49 (10), 1637–1648. https://doi.org/10.1071/eg984193a.
Pan, B., Sen, M.K., Gu, H., 2016. Joint inversion of PP and PS AVAZ data to estimate the fluid indicator in HTI medium: a case study in Western Sichuan Basin. China. J. Geophys. Eng. 13 (5), 690–703. https://doi.org/10.1088/1742-2132/13/5/690.
Pang, S., Liu, C., Guo, Z.Q., Liu, X.W., Liu, Y.W., 2018. Gas identification of shale reservoirs based on frequency-dependent AVO inversion of seismic data. Chin. J. Geophys. 61 (11), 4613–4624. https://doi.org/10.6038/cjg2018L0529 (in Chinese).
Partyka, G., 1999. Interpretational applications of spectral decomposition in reservoir characterization. Lead. Edge 18 (3), 353–360. https://doi.org/10.1190/1.1438295.
Qin, X., Gui, Z., Yang, F., Liu, Y., 2021. Anisotropic frequency-dependent characteristics of PP- and PS-waves in partially saturated double-porosity rocks. J. Geophys. Eng. 18 (3), 355–368. https://doi.org/10.1093/jge/gxab019.
Rapoport, M.B., Rapoport, L.I., Ryjkov, V.I., 2004. Direct detection of oil and gas fields based on seismic inelasticity effect. Lead. Edge 23 (3), 276–278. https://doi.org/10.1190/1.1690901.
Ren, H., Goloshubin, G., Hilterman, F., 2007. Spectra crossplot. Lead. Edge 26 (12), 1562–1566. https://doi.org/10.1190/1.2792410.
Ren, H., Goloshubin, G., Hilterman, F., 2009. Poroelastic analysis of permeability effects in thinly layered porous media. Geophysics 74 (6), N49–N54. https://doi.org/10.1190/1.3223185.
Russell, B., Hedlin, K., Hilterman, F., Lines, L., 2003. Fluid-property discrimination with AVO: a Biot-Gassmann perspective. Geophysics 68, 29–39. https://doi.org/10.1190/1.1543192.
Rüger, A., 2002. Reflection Coefficients and Azimuthal AVO Analysis in Anisotropic Media. The United State of America: Society of Exploration Geophysicists.
Shuey, R.T., 1985. Simplication of the Zoeppritz equation. Geophysics 50 (4), 609–614. https://doi.org/10.1190/1.1441936.
Sinha, S., Routh, P., Anno, P., 2009. Instantaneous spectral attributes using scales in continuous-wavelet transform. Geophysics 74 (2), WA137–WA142. https://doi.org/10.1190/1.3054145.
Smith, G.C., Gidlow, P.M., 1987. Weighted stacking for rock property estimation and detection of gas. Geophys. Prospect. 35, 993–1014. https://doi.org/10.1111/j.1365-2478.1987.tb00856.x.
Wei, X., Chen, T., Ji, Y., 2008. Converted wave AVO inversion for average velocity ratio and shear wave reflection coefficient. Appl. Geophys. 5 (1), 35–43. https://doi.org/10.1007/s11770-008-0010-x.
White, J.E., Mikhaylova, N.G., Lyakhovitskiy, F.M., 1976. Low-frequency seismic waves in fluid-saturated layered rocks. Phys. Solid Earth 11, 654–659. https://doi.org/10.1121/1.1995164.
Wilson, A., Chapman, M., Li, X.Y., 2009. Frequency-dependent AVO inversion. SEG Tech. Progr. Expand. Abstr. 341–345. https://doi.org/10.1190/1.3255572.
Wu, X., Chapman, M., Li, X., et al., 2015. Quantitative gas saturation estimation by frequency-dependent amplitude-versus-offset analysis. Geophys. Prospect. 62 (6), 1224–1237. https://doi.org/10.1111/1365-2478.12179.
Wu, X., Chapman, M., Wilson, A., Li, X.-Y., 2010. Estimating seismic dispersion from pre-stack data using frequency-dependent AVO inversion. SEG Tech. Progr. Expand. Abstr. 425–429. https://doi.org/10.1190/1.3513759.
Zhang, S., Yin, X., Zhang, G., 2011. Dispersion-dependent attribute and application in hydrocarbon detection. J. Geophys. Eng. 8 (4), 498–507. https://doi.org/10.1088/1742-2132/8/4/002.
Zhang, Z., Yin, X.Y., Hao, X.Q., 2014. Frequency-dependent fluid identification method based on AVO inversion. Chin. J. Geophys. 57 (12), 4171–4184. https://doi.org/10.6038/cjg20141228 (in Chinese).
Zong, Z., Yin, X., Wu, G., 2015. Complex seismic amplitude inversion for P-wave and S-wave quality factors. Geophys. J. Int. 202, 564–566. https://doi.org/10.1093/gji/ggv179.
Zong, Z., Yin, X., Wu, G., 2016. Frequency dependent elastic impedance inversion for interstratified dispersive elastic parameters. J. Appl. Geophys. 131, 84–93. https://doi.org/10.1016/j.jappgeo.2016.05.010.